J Arid Land (2026) 18(5): 735–751
doi: 10.1016/j.jaridl.2026.05.001; CSTR: 32276.14.JAL.20250338

Spatiotemporal dynamics and driving factors of carbon sinks across ecosystems in Northwest China

CHEN Xueye[1], SHI Ying[2], BIE Qiang[2*], Mujib ADEAGBO[3]

[1] Key Laboratory of Urban Land Resources Monitoring and Simulation, Ministry of Natural Resources, Shenzhen 518000, China;
[2] School of Geomatics, Lanzhou Jiaotong University, Lanzhou 730070, China;
[3] School of Engineering, Cardiff University, Cardiff CF243AA, UK

Abstract: Net ecosystem productivity (NEP) is a key indicator for estimating carbon sink dynamics in terrestrial ecosystems. Existing studies on carbon sink dynamics in Northwest China have uncertainties in quantifying spatiotemporal variations of NEP and their driving factors. This study estimated NEP across ecosystems in Northwest China during 2000–2020 using multi-model integration, and analyzed its spatiotemporal patterns and drivers. Results showed that the annual average NEP was 97.98 g $C/(m^2 \cdot a)$, with higher values at eastern and western margins and lower values in central hinterland. Strong carbon sink areas included the Yili River Basin and northern slope of Tianshan Mountains, while low carbon sink areas concentrated in eastern Xinjiang Uygur Autonomous Region (Eastern Xinjiang) and Alxa-Ejin Plateau. NEP trended upward from 79.22 g $C/(m^2 \cdot a)$ in 2000 to 109.03 g $C/(m^2 \cdot a)$ in 2020 with low variability and strong persistence, suggesting continuous growth. NEP significantly and positively correlated with near-infrared reflectance of vegetation (NIRv), weakly with climate factors, and negatively with socio-economic density indicators. Topographically, NEP peaked at 2.0–2.4 km elevation, 15°–25° slopes, and north-facing aspects. Changes in ecosystem type significantly influenced NEP, with bare land conversion into grassland/cropland enhancing carbon sinks. Results of this study highlight the need for ecological restoration and rational land use to boost carbon sequestration in this ecologically sensitive region.

Keywords: near-infrared reflectance of vegetation; net ecosystem productivity; carbon sink; driving factors; Northwest China

Citation: CHEN Xueye, SHI Ying, BIE Qiang, Mujib ADEAGBO. 2026. Spatiotemporal dynamics and driving factors of carbon sinks across ecosystems in Northwest China. Journal of Arid Land, 18(5): 735–751. https://doi.org/10.1016/j.jaridl.2026.05.001; https://cstr.cn/32276.14.JAL.20250338

1 Introduction

Carbon dioxide (CO_2), as a primary greenhouse gas, profoundly influences global climate change, land surface energy-water balance, and plant physiological processes (Friedlingstein et al., 2019). Terrestrial ecosystems in China play a critical role in carbon sequestration, offsetting approximately 21.0%–45.0% of the nation's annual fossil fuel CO_2 emissions and mitigating anthropogenic carbon burdens (Yue et al., 2024). Carbon sink, defined as the capacity to absorb and store atmospheric CO_2, is pivotal for global climate change mitigation (Leng et al., 2024). Among indicators quantifying carbon dynamics, net ecosystem productivity (NEP) serves as a

---

[*]Corresponding author: BIE Qiang (E-mail: bieq@lzjtu.edu.cn)

Received 2025-07-23; revised 2026-03-06; accepted 2026-03-15

http://jal.xjegi.com; https://www.keaipublishing.com/en/journals/journal-of-arid-land/

fundamental metric for assessing carbon sink/source functions, integrating gross primary productivity (GPP) and soil respiration processes.

Existing methodologies for NEP estimation include field-based carbon density measurements (Fang et al., 2007), process-based models (e.g., Carbon Exchange between Vegetation, Soil and Atmosphere, Boreal Ecosystem Productivity Simulator, and Biome Biogeochemical Cycle Model (Fang et al., 2024), and remote sensing-derived approaches (e.g., Carnegie-Ames-Stanford Approach (CASA)). The near-infrared reflectance of vegetation (NIRv) index, has emerged as a powerful tool in recent years, leveraging its sensitivity to vegetation fraction and soil reflectance to improve GPP estimation (Badgley et al., 2019; Ren et al., 2022). By incorporating soil background correction, the NIRv model further enhances pixel-level vegetation coverage representation, making it suitable for heterogeneous arid landscapes.

The arid region of Northwest China, characterized by a fragile ecological environment and complex interactions between climate and human activities, faces increasing CO_2 concentrations due to economic development. Despite its ecological significance, the region's carbon sink capacity remains poorly constrained, with multi-factor influences (e.g., climate variability, land use change) introducing substantial uncertainties.

This study aims to address these issues by estimating NEP across diverse ecosystems (2000–2020) in an integrated framework, including the soil-background-corrected NIRv model, Temperature and Evaporation Stress model and soil respiration model. Through trend analysis, fluctuation analysis, and correlation analysis, we systematically characterize spatiotemporal patterns of NEP and quantify the relative contributions of natural and anthropogenic drivers, thereby offering scientific support for carbon management in this ecologically vulnerable region. This multi-dimensional framework allows for the quantitative assessment of these two types of factors' relative impacts on NEP dynamics, thus yielding critical insights into the complex mechanisms underlying carbon sequestration in this ecologically vulnerable region.

2 Study area and data sources

2.1 Study area

The study area is located in Northwest China, which extends to the Helan Mountains in the east, the Pamir Plateau in the west, the Kunlun-Altun-Qilian mountains in the south, and the Altay Mountains in the north (34°25′–49°10′N, 73°40′–107°39′E; Fig. 1). The study area comprises eight sub-regions: Ertix-Ulungur River Basin, the northern slope of Tianshan Mountains, Yili River Basin, Tarim River Basin, eastern Xinjiang Uygur Autonomous Region (hereinafter referred to as Eastern Xinjiang), Hexi Corridor, Alxa-Ejin Plateau, and Yinchuan Plain (Geng et al., 2013) (Fig. 1). Covering an area of 2.15×10^6 km^2 with elevations ranging from –154 to 8545 m, the study area exhibits a temperate continental climate characterized by scarce precipitation due to its inland remoteness.

2.2 Data sources

Digital elevation model (DEM) data were derived from the Geospatial Data Cloud platform (http://www.gscloud.cn/), which were used to derive topographic parameters, including elevation, slope, and aspect. Meteorological data (evapotranspiration, temperature, and precipitation) were sourced from the National Tibetan Plateau Data Center (https://data.tpdc.ac.cn/). Vegetation classification relied on the 300-m resolution European Space Agency's Climate Change Initiative (ESA CCI)-Land Cover dataset (Harper et al., 2023). Remote sensing data incorporated several key products: MOD13A1 normalized difference vegetation index (NDVI) from National Aeronautics and Space Administration (NASA), utilized for calculating monthly NIRv values; MOD17A2H V6 GPP data, employed to validate both ground station measurements and our modeled (GPP) estimates (Ryu et al., 2011; Jiang and Ryu, 2016). The dataset of population density was sourced from the WorldPop Global Datasets (https://hub.worldpop.org/), and the

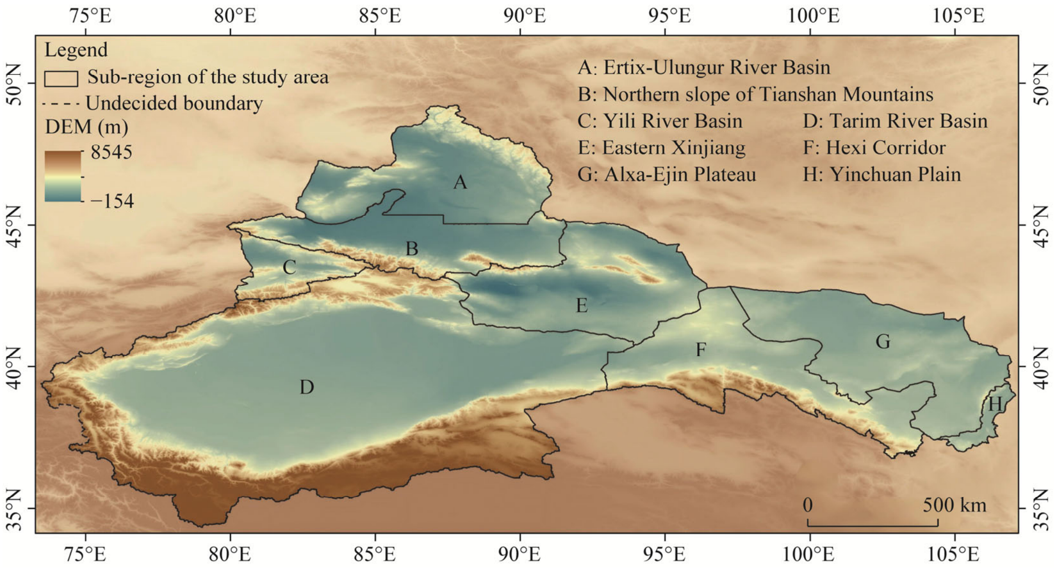

Fig. 1 Schematic map and eight sub-regions of in Northwest China. Eastern Xinjiang: eastern Xinjiang Uygur Autonomous Region. Note that the figure is based on the standard map (GS(2023)2767) of the National Geomatics Center of China (https://www.ngcc.cn/), and the boundary of the standard map has not been modified.

dataset of gross domestic product (GDP) was obtained from the Resources and Environment Science and Data Center (https://www.resdc.cn/). All Moderate Resolution Imaging Spectroradiometer (MODIS) products were radiometrically calibrated to correct the long-term sensor sensitivity degradation. Atmospheric noise was removed via the 6S (Second Simulation of the Satellite Signal in the Solar Spectrum) model, which has been validated to reduce NDVI bias by 8.0%–12.0% in hyper-arid regions (Chen et al., 2022). We exclusively used MODIS v.6.1 products, whose algorithm improvements address key limitations of earlier versions for arid regions. Terra MODIS provided continuous data. Aqua MODIS filled only 3.2% of gaps, with cross-sensor bias <3.0%. All spatial data were resampled to the baseline of 300 m (consistent with the ESA CCI land cover dataset) because ecosystem type is a core driver of NEP, and unifying to its resolution helps minimize mixed-pixel errors in ecological classification. The 90 m DEM was resampled to 300 m using bilinear interpolation, preserving gradient continuity and avoiding abrupt value jumps common in nearest-neighbor interpolation. The 1-km MODIS products were resampled to 300 m using bilinear interpolation, validated to retain vegetation signal integrity in arid regions, where sparse vegetation is sensitive to over-smoothing (Chen et al., 2022). All resampling was conducted in ENVI v.6.0 software, with projection unified to World Geodetic System 1984 (WGS84)/Universal Transverse Mercator (UTM) to ensure spatial alignment. Scale unification to 300 m does not distort NEP patterns or magnitudes, as the selected interpolation methods and baseline resolution align with the spatial heterogeneity of arid ecosystems (Zhang et al., 2022).

Soil carbon density data were obtained from the Spatio-Temporal Three-Pole Environment Big Data Platform (https://poles.tpdc.ac.cn/zh-hans/). Eddy covariance CO_2 flux measurements from 15 ecosystem sites (National Tibetan Plateau Data Center, National Ecological Data Center Sharing Service Platform, and ChinaFLUX) were used for validation (Zhang et al., 2023). The half-hourly NEE measurements were processed and aggregated into daily values for subsequent analysis. Detailed information of the 15 ecosystem sites is presented in Table 1. Relationship between these carbon flux components was established through the following equation: GPP= –GEE= –(NEE–ER), where GPP is the gross primary production (g C/(m^2·a)); GEE is the Gross Ecosystem Exchange (g C/(m^2·a)); NEE is the net ecosystem exchange (g C/(m^2·a)); and ER is the ecosystem respiration (g C/(m^2·a)). All datasets were standardized to a consistent spatial scale and temporal range (2000–2020).

Table 1 Information of the 15 ecosystem sites

Ecosystem type	Site name	Latitude	Longitude	Elevation (m)
Forest land	Sidaoqiao	42°00′00″N	101°08′24″E	873
	Sidalong	38°25′48″N	99°55′48″E	3146
	Dayekou Guantan Forest	38°31′48″N	100°15′00″E	2835
	Hunhelin	41°59′24″N	101°07′48″E	874
Grassland	Zhangye	38°58′48″N	100°27′00″E	1460
Cropland	Linze	39°19′48″N	100°08′24″E	1440
	Daman	38°51′36″N	100°22′12″E	1556
	Yingke Irrigation District Oasis	38°51′36″N	100°24′36″E	1519
	Nongtian	42°00′00″N	101°07′48″E	875
Barren land	Guazhou	41°24′36″N	95°40′12″E	2014
	Huazhaizi	38°46′12″N	100°19′12″E	1731
	Huangmo	42°06′36″N	100°59′24″E	1054
	Luodi	42°00′00″N	101°07′48″E	878
	Minqin	39°12′36″N	103°40′12″E	1020
	Shenshawo Desert	38°47′24″N	100°29′24″E	1594

3 Methodology

3.1 Vegetation NEP estimation model

NEP, a key metric for quantifying carbon source/sink dynamics in terrestrial ecosystems, is calculated through the balance between GPP and total ecosystem respiration (autotrophic respiration and heterotrophic respiration) (Woodwell et al., 1978). And the equation of NEP is as below:

$$\mathrm{NEP}=\mathrm{NPP}-R_{\mathrm{t}}=\mathrm{GPP}-R_{\mathrm{a}}-R_{\mathrm{h}}\,, \tag{1}$$

where NPP is the net primary production of vegetation (g C/(m^2·a)); R_{t} is the total ecosystem respiration (g C/(m^2·a)); R_{a} is the consumption of autotrophic respiration by vegetation (g C/(m^2·a)); and R_{h} is the heterotrophic respiration rate of the soil (g C/(m^2·a)).

NEP>0.00 indicates a carbon sink, where ecosystem carbon fixation exceeds soil carbon emissions, suggesting the ecosystem functions as a CO_2 sink. Conversely, NEP<0.00 denotes a net carbon source to the atmosphere. This conceptual framework provides clear operational definitions for source/sink characterization.

3.1.1 Estimation of GPP

Recent studies have demonstrated the widespread application of the NIRv as a robust proxy for estimating GPP across diverse spatiotemporal scales, ecosystem types, and climatic conditions (Shi et al., 2017; Ryu et al., 2019). Building upon previous research (Wu et al., 2020; Jiang et al., 2021), empirical evidence confirms a strong linear correlation between NIRv and GPP, while the soil-adjusted NIRv (SANIRv) exhibits a quantifiable proportional relationship with GPP (Jiang et al., 2021). These findings establish a theoretical foundation for enhancing the accuracy of GPP estimations. The formula is as below:

$$\mathrm{GPP}=c\times\mathrm{PAR}\times\mathrm{SANIRv}\,, \tag{2}$$

where c is the calibration coefficient; and PAR is the monthly photosynthetically active radiation (MJ/(m^2·d)). Calibration was performed using site-specific GPP observations, with ecosystems lacking data adopting the same c as barren land.

The accuracy of the estimated GPP results was evaluated through multiple cross-validations (80.0% training and 20.0% testing). The mean value of R^2 of multiple tests was used as the GPP estimation accuracy, with an overall R^2 of 0.7800 (P<0.01), as shown in Figure 2. We also compared estimated GPP from MOD17A2H and measured GPP as a control (Wu et al., 2020). Figure 3 showed that MOD17A2H overestimated the GPP in the study area. The results of the comparison of NIRv model are more accurate and reliable, and the GPP of the study area is representative and applicable.

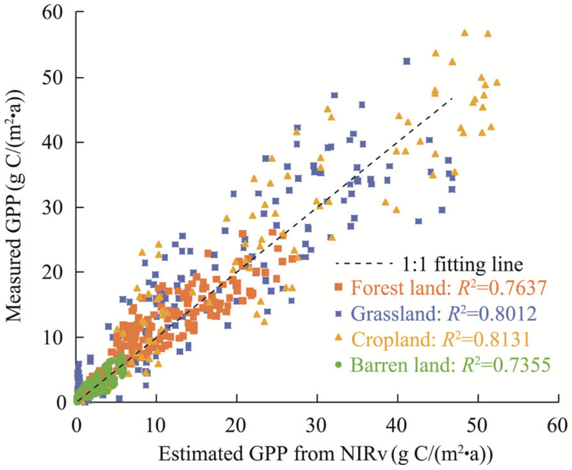

Fig. 2 Comparison of estimated gross primary production (GPP) from near-infrared reflectance of vegetation (NIRv) and measured GPP

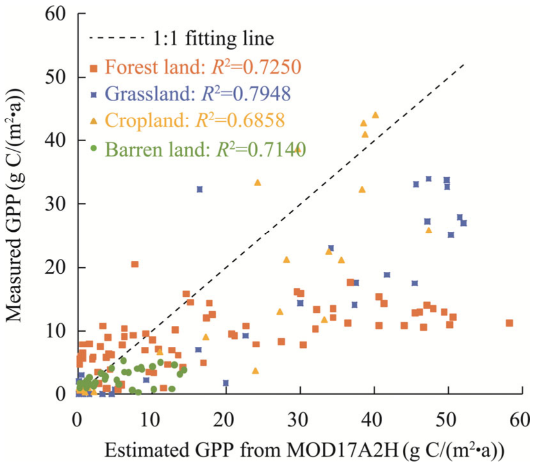

Fig. 3 Comparison of estimated GPP from MOD17A2H and measured GPP

3.1.2 Estimation of R_a in vegetation

Respiration is the process by which organic matter in living cells is gradually oxidized and decomposed under the action of enzymes and energy is released. R_a comprises vegetation growth respiration (R_g; g C/(m^2·a)) and maintenance respiration (R_m; g C/(m^2·a)). The R_g and R_m estimation are based on the method of Zhao and Running (2010), and the TEC (Terrestrial Ecosystem Carbon) model, i.e., the difference between GPP and R_a. The following equations are used to calculate R_a:

$$R_a = R_g + R_m\,, \tag{3}$$

$$R_g = r_g \times \mathrm{GPP}\,, \tag{4}$$

$$R_m = \sum_{i=1}^{3} M_i R_{m,i} Q_{10,i}^{(T-T_b)/10}\,, \tag{5}$$

$$M_i = \mathrm{LAI}/\mathrm{SLA}\ , \tag{6}$$

where r_g is the growth respiration coefficient, and r_g is 0.99 (Liu et al., 1997); i is the different organs of vegetation, i.e. leaves, stems, and roots (coarse roots, fine roots); M_i and $R_{m,i}$ are the biomass of the i^{th} organ (kg/m^2) and the respiration rate (g C/(m^2·a)) at the T_b temperature, which is the basal temperature of respiration, respectively; T is the average temperature (°C), and the value here is 25°C; $Q_{10,i}$ is the sensitivity factor of the i^{th} organ to temperature changes in respiration (Arora, 2003); LAI is the leaf area index; and SLA is the specific leaf area (m^2/kg), which aims to realize the conversion of biomass and leaf area index. $Q_{10,i}$ is calculated by Equation 7:

$$Q_{10,i} = 3.22 - 0.046T\ . \tag{7}$$

For the values of vegetation parameters, refer to the Boreal Ecosystem Productivity Simulator (BEPS) and Biome-BioGeochemical Cycles (Biome-BGC) models, as shown in Table 2. R_m of ecosystems for grassland and farmland is a function of LAI and temperature (Hu et al., 2011), as shown below:

$$R_m = 1.0368\mathrm{LAI} \times 2^{0.1(T-T_b)} / 1000\ . \tag{8}$$

Table 2 Vegetation parameters

Vegetation parameter	Evergreen forest	Deciduous forest	Mixed forest	Other forests
SLA (m^2/kg)	10	25	17	25
$R_{m,1}$ (g C/(m^2·a))	0.0020	0.0060	0.0040	0.0080
$R_{m,2}$ (g C/(m^2·a))	0.0010	0.0010	0.0010	0.0010
$R_{m,3}$ (g C/(m^2·a)) (coarse root)	0.0010	0.0010	0.0010	0.0015
$R_{m,3}$ (g C/(m^2·a)) (fine root)	0.0030	0.0030	0.0030	0.0015
$Q_{10,1}$	2.1	2.1	2.1	2.1
$Q_{10,2}$	1.7	1.3	1.5	1.5
$Q_{10,3}$	1.9	1.9	1.9	1.9
M_2 (kg/m^2)	10.1	8.8	8.1	1.0
M_3 (kg/m^2)	$0.2317M_2$	$e^{0.359}M_2^{\ 0.639}$	$0.5\left(0.2317M_2 + e^{0.359}M_2^{\ 0.639}\right)$	0.2

Note: SLA, specific leaf area; $R_{m,1}$, $R_{m,2}$, and $R_{m,3}$ are the respiration rates of leaves, stems, and roots, respectively; $Q_{10,1}$, $Q_{10,2}$, and $Q_{10,3}$ are the sensitivity factors of leaves, stems, and roots, respectively; M_2 and M_3 are the biomass of stems and roots, respectively.

3.1.3 Estimation of soil R_h

R_h (kg C/(m^2·a)) was derived from soil respiration (R_s; kg C/(m^2·a)) using a power function regression (Xie et al., 2014) as follows:

$$R_h = 0.6163R_s^{0.7918}\ , \tag{9}$$

$$R_s = R_0 e^{Q\times T} \times P/(P+K) \times \mathrm{SOC}/(\mathrm{SOC}+\psi)\ , \tag{10}$$

where P is the annual precipitation (mm); SOC is the organic carbon density of surface soil (0–20 cm) (kg C/m^2); R_0, Q, K, and Ψ are model parameters, which represent SOC content without precipitation and carbon storage limitation (kg SOC/(m^2·a)), the coefficient determining the exponential relationship between soil respiration and temperature (°C), the semi-saturation constant of the hyperbolic relationship between soil respiration and annual precipitation (m), and the semi-saturation constant of the Michaelis-Menten equation of soil respiration and SOC content (kg C/m^2), respectively (Table 3) (Janssen and Heuberger, 1995; Raich et al., 2002; Chen et al., 2010).

3.2 Validation of NEP results

The accuracy of the NEP model is verified by comparing it with the measured data from 15 flux

Table 3 Specific parameters of estimating R_s

Parameter	Cropland	Grassland	Forest land	Barren land and others
R_0 (kg SOC/(m^2•a))	4.63±2.14	9.62±6.70	1.34±0.17	1.55±0.17
Q (°C)	0.004±0.015	0.023±0.007	0.029±0.004	0.031±0.003
K (m)	1.94±0.98	5.16±3.89	0.59±0.14	0.68±0.12
Ψ (kg C/m^2)	4.27±1.21	3.99±1.66	1.43±0.33	2.23±0.34

Note: R_s, soil respiration; R_0, soil organic carbon (SOC) content without precipitation and carbon storage limitation; Q, coefficient determining the exponential relationship between soil respiration and temperature; K, semi-saturation constant of the hyperbolic relationship between soil respiration and annual precipitation; Ψ, semi-saturation constant of the Michaelis-Menten equation of soil respiration and SOC content. Mean±SE.

stations, which were carefully selected to cover the four core ecosystem types (forest land, grassland, cropland, and barren land) and sub-regions in the study area (Table 1), ensuring spatial and ecological representativeness. This coverage aligns with the "ecosystem-type priority" validation strategy, widely used in carbon models in arid regions, where capturing functional differences between ecosystems is more critical than uniform spatial density (Zhang et al., 2023). The estimated NEP showed strong agreement with measured values (R^2=0.8537, P<0.01; Fig. 4), confirming model reliability.

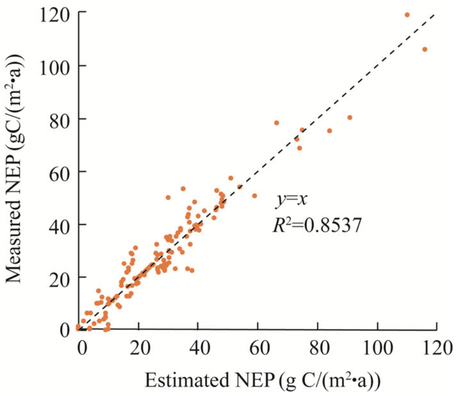

Fig. 4 Comparison of estimated net ecosystem productivity (NEP) and measured NEP

3.3 Methods of analysis

3.3.1 Trend analysis

Univariate linear regression was applied to quantify NEP trends, with the slope reflecting inter-annual changes (Zhang et al., 2021). Slope>0 indicates increasing NEP, and slope<0 indicates decreasing NEP, while slope=0 denotes stability.

3.3.2 Fluctuation analysis

In order to study the relative change of NEP in the study area during 2000–2020, we used the coefficient of variation (CV) to assess the inter-annual stability of NEP.

3.3.3 Temporal trend continuity analysis

The Hurst index (H) was calculated via the Rescaled Range Analysis method to evaluate trend continuity (Hurst, 1951). The range of H value is between 0.00 and 1.00, and it was divided into four categories: strong anti-persistence (H≤0.35), weak anti-persistence (0.35<H≤0.50), weak persistence (0.50<H≤0.65), and strong persistence (H>0.65).

3.3.4 Cluster analysis

Local spatial clustering of NEP was analyzed using Anselin Local Moran's I and Getis-Ord Gi* statistics (Anselin, 1995). Four spatial association patterns were identified: HH (high–high), HL (high–low), LH (low–high), and LL (low–low) clusters. Non-significant cluster (NS) was defined as areas with no statistically significant spatial association. The Moran's I statistic ranges from –1 to 1, where $I>0$ indicates positive spatial autocorrelation, $I<0$ indicates negative autocorrelation, and $I=0$ signifies random distribution.

3.3.5 Correlation analysis

Pearson correlation analysis was performed to quantify relationships between NEP and influencing factors (e.g., temperature, precipitation, and NIRv) at the pixel scale. Statistical significance was evaluated using *t*-tests.

4 Results

4.1 Spatial evolution characteristics of NEP

4.1.1 Spatial distribution of NEP

The spatial distribution of annual average NEP in the study area over the past 21 a is shown in Figure 5. The annual average NEP in the study area was 97.98 g C/(m^2·a), exhibiting a distinct spatial pattern of "higher values at eastern and western margins, lower values in central hinterland". Strong carbon sink areas (annual average NEP>200.00 g C/(m^2·a)) included the Yili River Basin (765.44 g C/(m^2·a)), northern slope of Tianshan Mountains (232.48 g C/(m^2·a), Yinchuan Plain (223.1 g C/(m^2·a)), and Ertix-Ulungur River Basin (221.10 g C/(m^2·a)), characterized by favorable hydrothermal conditions and high vegetation coverage. Moderate carbon sink areas, such as the Hexi Corridor (78.21 g C/(m^2·a)) and Tarim River Basin (55.93 g C/(m^2·a)), were constrained by water resource distribution and oasis agriculture. Low carbon sink areas, including Eastern Xinjiang (34.08 g C/(m^2·a)) and the Alxa-Ejin Plateau (12.90 g C/(m^2·a)), were dominated by desert and sparse vegetation. Carbon sources were sparsely distributed in small areas in the Tarim River Basin and northern Ertix-Ulungur River Basin.

Spatial autocorrelation analysis revealed significant clustering of NEP values (Fig. 6). HH clusters, accounting for 50.9% of the area, were concentrated in the Yili River Basin and northern slope of Tianshan Mountains, where dense vegetation and stable ecosystems prevailed. These zones are ecological "carbon sink core zones" and driven by optimal water-heat matching and high vegetation coverage. LL clusters (48.8%) were mainly distributed in the southern Ertix-Ulungur River Basin and Alxa-Ejin Plateau. These zones are "carbon sink fragile zones" and constrained by extreme aridity and sparse vegetation. Annual precipitation here is <100 mm, and potential evapotranspiration exceeds 2000 mm, creating a severe water deficit that limits vegetation growth (vegetation coverage is <15.0% with mostly desert shrubs and annual herbs). HL and LH clusters comprised less than 1.0%, indicating that spatial heterogeneity was driven by contiguous distribution of similar ecosystems.

4.1.2 Inter-annual spatial variation of NEP

The range of NEP changed from –700.73 to 1365.00 g C/(m^2·a), with an overall 71.5% increasing

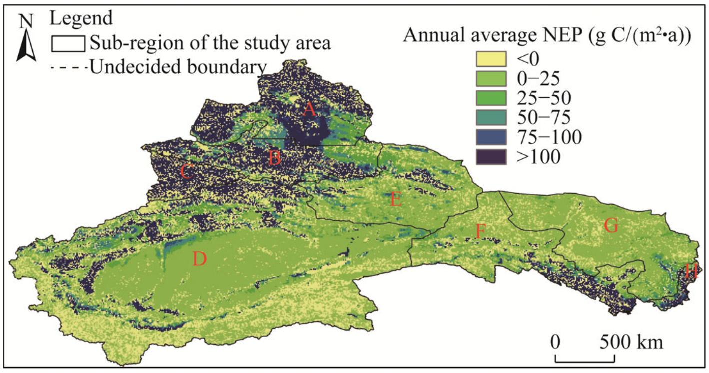

Fig. 5 Spatial distribution of annual average NEP during 2000–2020

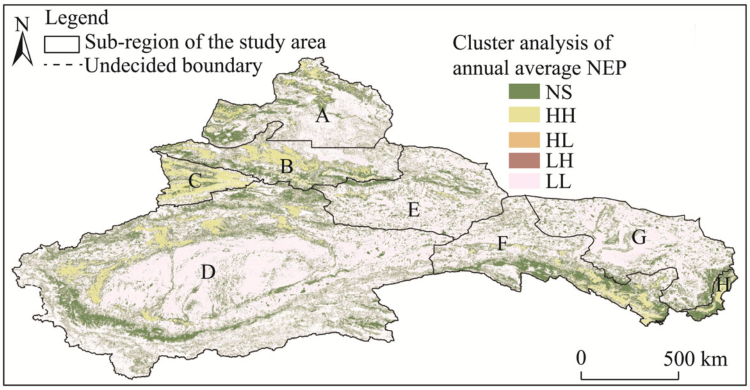

Fig. 6 Cluster analysis of annual average NEP during 2000–2020. NS, non-significant cluster; HH, high–high; HL, high–low; LH, low–high; LL, low–low.

trend in the area. The most obvious increases occurred in the northern slope of Tianshan Mountains, southern Hexi Corridor, northeastern Tarim River Basin, and Yinchuan Plain, reflecting improved vegetation coverage and ecological conditions over the past 21 a.

Classified by slope of trend lines (Fig. 7), non-significant increase areas accounted for 44.1%, the largest proportion among growing areas. Significant (9.6%) and extremely significant (17.8%) increasing areas were primarily distributed in northern desert grassland and mountainous forest land with minimal human disturbance. Decreasing areas (28.5%) were mainly concentrated in Eastern Xinjiang and parts of the Yili River Basin, likely due to vegetation degradation caused by overgrazing, land reclamation, and mineral resource development.

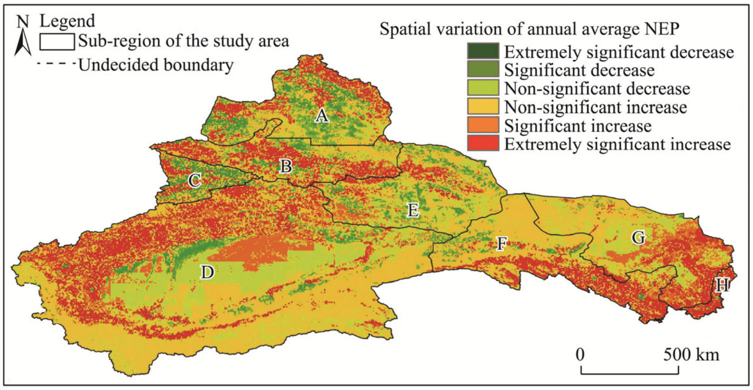

Fig. 7 Spatial variation of annual average NEP during 2000–2020

4.2 Temporal evolution characteristics of NEP

4.2.1 Inter-annual variation of NEP

During 2000–2020, the annual average NEP in the arid Northwest China was 97.98 g C/(m^2·a), with an increasing trend from 79.22 g C/(m^2·a) in 2000 to 109.03 g C/(m^2·a) in 2020, corresponding to an average annual growth rate of 1.49 g C/(m^2·a). As shown in Figure 8, NEP exhibited low inter-annual variability, with a CV ranging from 0.0 to 0.4. Spatially, stability was higher in the northern and southern margins (Ertix-Ulungur River Basin) and lower in central hinterland (Tarim River Basin). Areas with low stability ($CV \leq 0.1$) and relatively low stability ($0.1 < CV \leq 0.2$) accounted for 46.0%, primarily overlapping with areas of low vegetation cover and minimal ecosystem type changes, such as barren land. In contrast, high stability areas ($CV > 0.3$) comprising 46.2%, were dominated by forest land and grassland.

Temporal persistence analysis using the *H* index revealed that 94.4% of the area exhibited persistent trends (Fig. 9). It is important to emphasize that this persistence conclusion is premised on the current climate and human disturbance patterns remaining unchanged, as it only reflects the inertia of historical trends and cannot predict future systemic disturbances or nonlinear responses to climate change. The average *H* value was 0.64, indicating strong continuity of upward NEP trend. Strong persistence (H>0.65) occurred in 42.4% of the area, mainly in the north-central Tarim River Basin, while weak persistence (0.50<H≤0.65) covered 52.0%, largely coinciding with barren land areas. Only 5.6% of the area showed anti-persistence, with scattered distributions in Eastern Xinjiang and the Alxa-Ejin Plateau, suggesting limited likelihood of trend reversal.

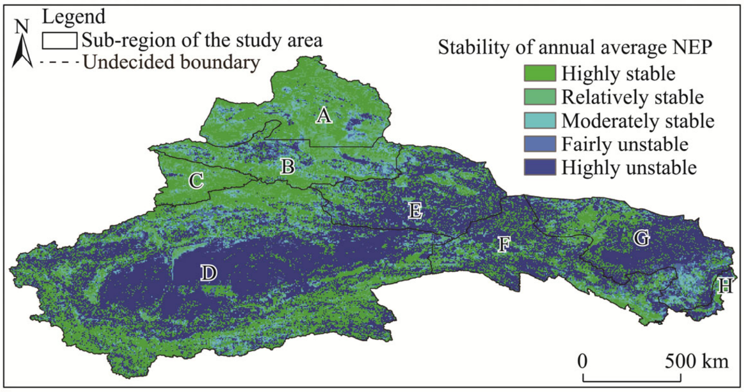

Fig. 8 Stability of annual average NEP during 2000–2020

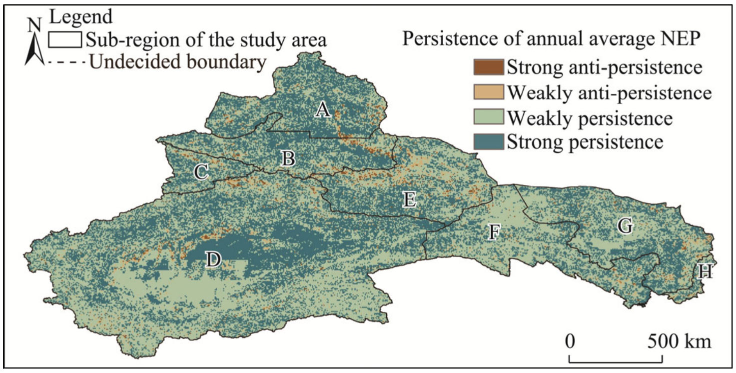

Fig. 9 Persistence of average annual NEP during 2000–2020

4.2.2 Intra-annual dynamics of NEP

The monthly NEP distribution exhibited significant spatial heterogeneity and seasonal patterns (Fig. 10). The annual trend of NEP could be divided into three stages. The first stage was the growth period (January–April), in which NEP increased continuously with rising temperatures and vegetation regrowth, particularly evident in April as photosynthesis intensified. The second stage was the high-value period (May–August), during which NEP maintained a high level and reached the peak in July, coinciding with optimal hydrothermal conditions and vigorous vegetation growth. The third stage was the decline period (September–December), during which NEP decreased progressively due to cooling temperatures and vegetation senescence, with respiration dominating over photosynthesis. Overall, NEP values were consistently higher in summer than in other seasons, reflecting the critical role of the temperature and radiation in regulating carbon sequestration. Monthly variations were more pronounced in forest land and grassland, while barren land showed minimal seasonal fluctuations.

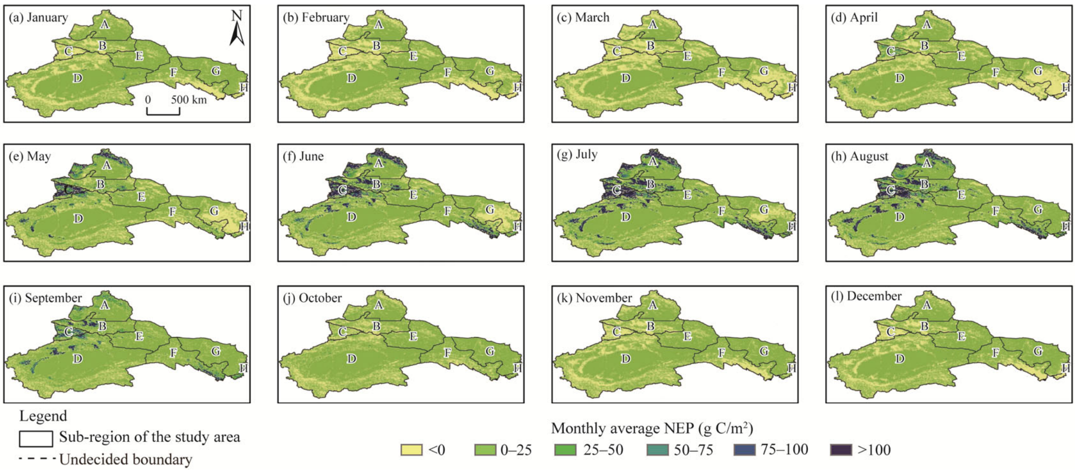

Fig. 10 Spatial distribution of monthly average NEP during 2000–2020. (a), January; (b), February; (c), March; (d), April; (e), May; (f), June; (g), July; (h), August; (i), September; (j), October; (k), November; (l), December.

5 Discussion

5.1 Spatiotemporal variation characteristics of NEP

The spatiotemporal dynamics of NEP in arid Northwest China reflect a complex interplay of climate, topography, and human activities, consistent with the multi-model framework and regional ecological characteristics established in the methodology and results sections. The trend of annual NEP increased from 79.22 g C/(m^2·a) in 2000 to 109.03 g C/(m^2·a) in 2020 (average annual growth rate was 1.49 g C/(m^2·a)), which aligns with the remote sensing-based estimations and ground validation, highlighting the robustness of soil-background-corrected NIRv model and TEC model (Badgley et al., 2017). This upward trajectory is attributed to vegetation recovery in ecologically restored areas and moderate warming trend in the area, which likely enhanced photosynthetic efficiency across grassland and cropland (Piao et al., 2020).

Spatially, the "high at eastern/western margins and low in central hinterland" pattern (Fig. 5) is consistent with the study area's hydrological and topographic gradients. Strong carbon sinks in the Yili River Basin (765.44 g C/(m^2·a)) and northern slope of Tianshan Mountains (232.48 g C/(m^2·a)) are driven by mountainous microclimates that sustain high vegetation coverage, while water-limited areas like the Tarim River Basin (55.93 g C/(m^2·a)) exhibit moderate carbon sequestration capacity due to oasis agriculture and sporadic vegetation (Jiang et al., 2020). The Alxa-Ejin Plateau (12.90 g C/(m^2·a)) and Eastern Xinjiang (34.08 g C/(m^2·a)), dominated by hyper-arid deserts, represent low-carbon sink zones, a finding corroborated by soil carbon density data and land cover classifications (Tu et al., 2023).

Spatial autocorrelation analysis (Fig. 6) revealed that 50.9% of the area exhibited HH cluster in stable ecosystems like mountainous forest land, while 48.8% of LL cluster occurred in barren landscapes with minimal vegetation connectivity. The scarcity of HL and LH clusters (<1.0%) reinforces the dominance of homogeneous land cover in shaping NEP patterns, a key insight supported by the study's focus on ecosystem type transitions (Xu et al., 2018). The HH or LL aggregation patterns provide clear spatial guidance for targeted ecological management in arid Northwest China. As the core of regional carbon sinks, HH cluster zones require strict protection of existing ecosystems to avoid degradation. LL cluster zones need targeted ecological restoration to enhance carbon sink, such as desertification control, water resource optimization, and restricting high-disturbance activities (Min et al., 2025).

Temporal trend analysis (Fig. 7) showed that NEP increased in 71.5% of the area, with significant growth in northern slope of Tianshan Mountains and southern Hexi Corridor, areas characterized by reduced human disturbance and successful ecological restoration projects (Li et al., 2021). Conversely, NEP declined in Eastern Xinjiang (linked to overgrazing) and parts of the Yili River Basin (attributed to mineral resource development), which highlighted the vulnerability of arid ecosystems to anthropogenic pressures (Min et al., 2025; Wang et al., 2025). The *H* index (H=0.64) confirmed strong temporal persistence in NEP trends, suggesting that current carbon sink dynamics might continue under stable climatic and policy conditions (Hurst, 1951). If future systemic disturbances occur, such as extreme drought or large-scale anthropogenic activities, the nonlinear response of arid ecosystems (e.g., sudden vegetation degradation and soil carbon loss) may break the current trend, leading to NEP declines or even trend reversal. This uncertainty highlights the need for long-term monitoring of climate and human activity changes to dynamically adjust carbon sink management strategies (Piao et al., 2020).

5.2 Influencing factors of NEP

The drivers of NEP in arid Northwest China exhibit a hierarchical interplay of biophysical and anthropogenic factors, as quantified by Pearson's correlation analysis and geodetector models (Fig. 11). Vegetation activity, represented by the NIRv, emerged as the primary determinant, showing a highly significant and positive correlation with NEP (P<0.01) and explaining 86.5% of its variability. This result aligns with the NIRv model's design, which captures canopy photosynthetic capacity by integrating soil background correction, making it particularly suitable for heterogeneous arid landscapes (Jiang et al., 2021). The strong association between NIRv and NEP underscores the critical role of vegetation coverage and productivity in regulating carbon sinks, consistent with global studies linking vegetation greenness to gross primary production.

Climate factors (temperature, precipitation, and potential evapotranspiration) exhibited weak positive but non-significant correlations with NEP, reflecting the complex hydrological constraints in water-limited ecosystems. While increased precipitation theoretically enhances soil moisture and photosynthesis, its impact was diluted by spatial heterogeneity in water availability (e.g., oasis vs. desert regions) and the dominance of NIRv-driven vegetation dynamics (Kolby Smith et al., 2016). Temperature, though influencing respiration rates, showed no significant trend, possibly due to countervailing effects of warming on vegetation growth and soil carbon loss (Mahecha et al., 2010).

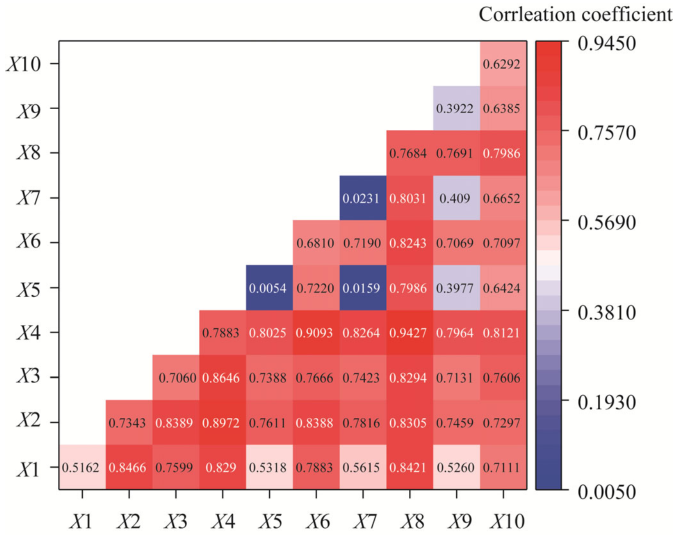

Fig. 11 Interactive detector of influencing factors. *X*1–*X*10 represent evapotranspiration, precipitation, temperature, NIRv, aspect, elevation, slope, ecosystem type, gross domestic product (GDP), and population density, respectively.

Topographic factors exerted nuanced effects. NEP peaked at elevations of 2.0–2.4 km, slopes of 15°–25°, and north-facing aspects. These patterns likely reflect optimal balances of solar radiation, soil moisture, and temperature on shaded slopes, which reduce evapotranspiration and favor moisture-sensitive vegetation (Bennie et al., 2008). For example, north-facing slopes in the Tianshan Mountains sustain higher vegetation cover by minimizing direct sunlight and preserving snowmelt water, whereas flat or south-facing areas suffer from intense evaporation and desertification (Zhang et al., 2022).

Socioeconomic indicators (population density and gross domestic product (GDP)) exhibited weakly negative correlations with NEP, indicating human activities degrade carbon sinks through land use change. Areas with high population density (e.g., oases in the Tarim River Basin) experienced intensified agriculture and urban expansion, leading to grassland conversion and soil carbon depletion (Zhang et al., 2022). Resource-intensive industries (e.g., coal mining in Eastern Xinjiang) further exacerbated vegetation loss, as evidenced by NEP declines in these areas (Zhang et al., 2022). For factors of human activities, we selected GDP and population density as proxies, which are widely used in carbon cycle studies in arid regions for their ability to capture large-scale human disturbances (Li et al., 2021; Zhang et al., 2022). We recognize that more direct indicators (e.g., nighttime light data for energy consumption and land use intensity index for ecosystem modification) could refine human activity quantification, which will be the focus of future research.

Interactive effects between factors (Fig. 11) revealed that the combined influence of ecosystem type and NIRv had the strongest enhancement effect on NEP, highlighting the synergistic role of vegetation structure and photosynthetic activity. Precipitation and temperature exhibited the strongest positive synergy on NEP when annual precipitation ranged from 200 to 400 mm and annual average temperature ranged from 8°C to 12°C (consistent with HH cluster of NEP in the Yili River Basin and northern slope of Tianshan Mountains). In this range, precipitation met vegetation water demand without leaching nutrients, while temperature optimized photosynthetic enzyme activity, jointly boosting NIRv and GPP (Li et al., 2021). In contrast, slope and aspect showed negligible interactive effects, suggesting their influence was primarily indirect, via microclimatic regulation (Bennie et al., 2008). These findings reinforce the importance of preserving intact ecosystems and reducing land-use intensity to sustain carbon sequestration in arid regions (Li et al., 2023).

5.3 Carbon sequestration capacities among different ecosystems

The carbon sequestration capacity of ecosystems in arid Northwest China varied significantly, driven by vegetation structure, productivity, and spatial extent (Fig. 12). Forest land exhibited the highest NEP (544.49 g C/(m^2·a)), attributed to their dense canopy structure and prolonged growing seasons, which maximized carbon uptake through photosynthesis (Yu et al., 2014). Cropland followed closely (516.00 g C/(m^2·a)), benefiting from human-managed water and nutrient inputs, though their carbon storage was often transient due to seasonal harvests. Grassland, despite lower productivity (165.00 g C/(m^2·a)), contributed the largest total NEP (9.44×10^{13} g C) owing to their extensive coverage (over 40.0% of the study area), highlighting the importance of ecosystem area in cumulative carbon accounting (Scurlock and Hall, 1998).

Barren land, though comprising over 60.0% of the area, displayed the lowest average NEP (23.12 g C/(m^2·a)), reflecting minimal vegetation activity and high soil carbon vulnerability (Fig. 12). The paradox of barren land contributing moderately to total NEP (3.14×10^{13} g C) underscores the trade-off between low productivity and vast spatial extent, emphasizing the need for targeted restoration in these regions to enhance regional carbon sinks (Reynolds et al., 2007).

Ecosystem transitions significantly influenced NEP dynamics. The conversion of barren land to grassland or cropland (e.g., through ecological engineering projects) was a key driver of NEP growth, with soil carbon gains from vegetation establishment outweighing initial carbon losses (Deng et al., 2017). Conversely, the degradation of grassland and forest land to barren land, primarily due to overgrazing and unsustainable land use reduced carbon sequestration capacity, particularly in semi-arid regions (Bestelmeyer et al., 2015).

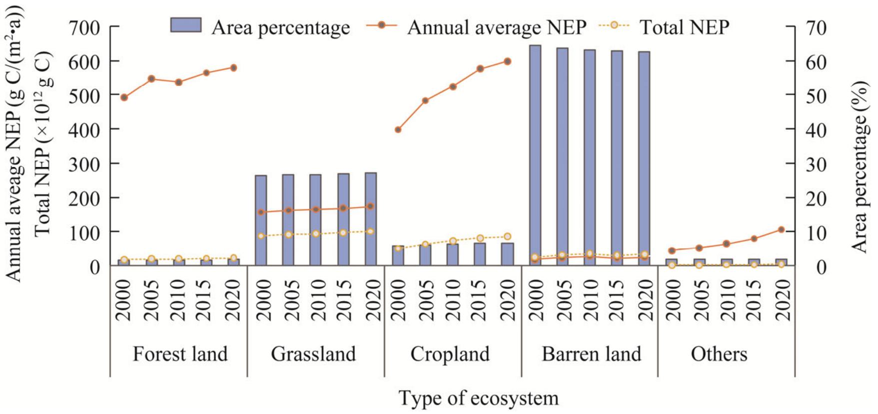

Fig. 12 Annual average NEP, total NEP, and area percentage of different types of ecosystem during 2000–2020

Mature forest land posed a unique challenge, i.e., while they currently act as strong carbon sinks, their sensitivity to climate variability (e.g., drought) and aging processes may limit future carbon uptake (Leng et al., 2024). This result highlights the importance of diversifying forest management strategies, such as introducing drought-resistant species to enhance long-term resilience (Grossiord et al., 2020).

5.4 Limitations

NEP estimation methods have evolved into three primary categories: process-based models, remote sensing-driven models, and field-based single-site observation. However, these methods often face limitations when they are applied to arid Northwest China, characterized by heterogeneous land surfaces (e.g., mixed bare soil and sparse vegetation), strong water-heat constraints, and limited observation data. For example, Biome-BGC assumes sufficient soil moisture for vegetation growth, which deviates from the "water-limited" reality of our study area, leading to overestimation of GPP by 15.0%–25.0% in hyper-arid regions (Jiang et al., 2021). Additionally, these models require high-resolution input data (e.g., hourly meteorology) that are scarce in remote arid regions, increasing parameterization uncertainty. Traditional remote sensing models (e.g., CASA) estimate NEP using NDVI or uncorrected NIRv as proxies for vegetation activity. When data availability is high, these models fail to account for soil background interference—a critical issue in arid regions where bare soil contributes 60.0%–80.0% of surface reflectance (Ren et al., 2022), which leads to underestimation of GPP in sparse vegetation regions (e.g., desert grassland) by 10.0%–20.0% (Wu et al., 2020). MOD17A2H, for instance, shows a lower validation R^2 (0.6858–0.7948; Fig. 3) in our study area compared with soil-corrected NIRv model (R^2=0.7800; Fig. 2), particularly in the Alxa-Ejin Plateau (bare soil-dominated). Field-based observations (e.g., eddy covariance flux towers) provide high-accuracy NEP data but suffer from poor spatial representativeness. In the study area, only 15 flux stations exist (Table 1), and most are concentrated in oases or mountainous forest land—failing to cover hyper-arid desert or sparse grassland.

Although the study has the above limitations, we improved the certainty of the result through three aspects: (1) soil-background-corrected NIRv for GPP estimation, by which removing bare soil reflectance interference; (2) multi-model synergy for respiration quantification. The TEC model explicitly incorporates water–heat limitations in arid region to estimate autotrophic respiration, while a power-function model links R_s to R_h, avoiding the "one-size-fits-all" parameterization of process-based models; and (3) regional scalability with multi-resolution data fusion, by which framework balances accuracy and spatial coverage, overcoming the scale gap between single-site observation and coarse-resolution remote sensing models.

6 Conclusions

This study systematically analyzed the spatiotemporal dynamics of NEP in arid Northwest China during 2000–2020. The results revealed distinct spatial patterns of NEP, with strong carbon sinks distributed in ecologically favorable areas and low-carbon sink areas concentrated in hyper-arid regions constrained by sparse vegetation. NEP showed a significant upward trend with high temporal persistence, indicating sustained carbon sequestration potential under current ecological conditions. The NIRv was identified as the primary driver of NEP, while ecosystem transitions (notably barren land conversion to grassland or cropland) and topographic conditions (elevation, slope, and aspect) also exerted notable influences by shaping microclimatic suitability for vegetation growth.

The findings emphasize the critical role of ecological restoration and rational land management in enhancing regional carbon sink capacity. Targeted interventions—including desertification control, sustainable agricultural practices, and reduced anthropogenic disturbances in low NEP regions—are essential to mitigate land degradation and strengthen ecosystem resilience. The integrated framework of remote sensing data and process-based models established in this study provides a robust tool for quantifying carbon dynamics in data-scarce arid regions, offering insights for formulating regional climate change mitigation strategies. By linking NEP patterns to both natural drivers and human activities, this research highlights the importance of preserving intact ecosystems and adopting adaptive management practices to sustainably boost carbon sequestration in this ecologically vulnerable region of China.

Conflict of interest

The authors declare that they have no known competing financial interests or personal relationships that could have appeared to influence the work reported in this paper.

Acknowledgements

This research was supported by the Key Laboratory of Urban Land Resources Monitoring and Simulation, Ministry of Natural Resources (KF20230801) and the National Natural Science Foundation of China (42101096).

Author contributions

Methodology, formal analysis, and conceptualization: CHEN Xueye; Writing - review and editing, methodology, formal analysis, and conceptualization: SHI Ying; Supervision, funding acquisition, and conceptualization: BIE Qiang; Methodology and data curation: Mujib ADEAGBO. All authors approved the manuscript.

References

Anselin L. 1995. Local indicators of spatial association—LISA. Geographical Analysis, 27(2): 93–115.

Arora V K. 2003. Simulating energy and carbon fluxes over winter wheat using coupled land surface and terrestrial ecosystem models. Agricultural and Forest Meteorology, 118(1–2): 21–47.

Badgley G, Field C B, Berry J A. 2017. Canopy near-infrared reflectance and terrestrial photosynthesis. Science Advances, 3(3): e1602244, doi: 10.1126/sciadv.1602244.

Badgley G, Anderegg L D L, Berry J A, et al. 2019. Terrestrial gross primary production: Using NIR_V to scale from site to globe. Global Change Biology, 25(11): 3731–3740.

Bennie J, Huntley B, Wiltshire A, et al. 2008. Slope, aspect and climate: Spatially explicit and implicit models of topographic microclimate in chalk grassland. Ecological Modelling, 216(1): 47–59.

Bestelmeyer B T, Okin G S, Duniway M C, et al. 2015. Desertification, land use, and the transformation of global drylands. Frontiers in Ecology and the Environment, 13(1): 28–36.

Chen R, Yin G F, Zhao W, et al. 2022. TCNIRv: Topographically corrected near-infrared reflectance of vegetation for tracking gross primary production over mountainous areas. IEEE Transactions on Geoscience and Remote Sensing, 60: 1–10.

Chen S T, Huang Y, Zou J W, et al. 2010. Modeling interannual variability of global soil respiration from climate and soil properties. Agricultural and Forest Meteorology, 150(4): 590–605.

Deng L, Liu S G, Kim D G, et al. 2017. Past and future carbon sequestration benefits of China's grain for green program. Global

Environmental Change, 47: 13–20.

Fang J Y, Guo Z D, Piao S L, et al. 2007. Terrestrial vegetation carbon sinks in China, 1981–2000. Science in China Series D: Earth Sciences, 50(9): 1341–1350.

Fang M Z, Cheng C J, He N P, et al. 2024. Implication of community-level ecophysiological parameterization to modelling ecosystem productivity: A case study across nine contrasting forest sites in eastern China. Journal of Forestry Research, 35(1): 7, doi: 10.1007/s11676-023-01650-1.

Friedlingstein P, Jones M W, O'Sullivan M, et al. 2019. Global carbon budget 2019. Earth System Science Data, 11(4): 1783–1838.

Geng Q L, Wu P T, Zhang Q F, et al. 2013. Dry/wet climate zoning and delimitation of arid areas of Northwest China based on a data-driven fashion. Journal of Arid Land, 6(3): 287–299.

Grossiord C, Buckley T N, Cernusak L A, et al. 2020. Plant responses to rising vapor pressure deficit. New Phytologist, 226(6): 1550–1566.

Harper K L, Lamarche C, Hartley A, et al. 2023. A 29-year time series of annual 300 m resolution plant-functional-type maps for climate models. Earth System Science Data, 15(3): 1465–1499.

Hu B, Sun R, Chen Y J, et al. 2011. Estimation of ecosystem productivity in the Huang-Huai-Hai Region using remote sensing data combined with the Biome-BGC model. Journal of Natural Resources, 26(12): 2061–2071. (in Chinese)

Hurst H E. 1951. Long-term storage capacity of reservoirs. Transactions of the American Society of Civil Engineers, 116(1): 770–799.

Janssen P H M, Heuberger P S C. 1995. Calibration of process-oriented models. Ecological Modelling, 83(1–2): 55–66.

Jiang C, Guan K, Wu G, et al. 2021. A daily, 250 m and real-time gross primary productivity product (2000–present) covering the contiguous United States. Earth System Science Data, 13(2): 281–298.

Jiang C Y, Ryu Y. 2016. Multi-scale evaluation of global gross primary productivity and evapotranspiration products derived from Breathing Earth System Simulator (BESS). Remote Sensing of Environment, 186: 528–547.

Jiang S Z, Liang C, Cui N B, et al. 2020. Water use efficiency and its drivers in four typical agroecosystems based on flux tower measurements. Agricultural and Forest Meteorology, 295: 108200, doi: 10.1016/j.agrformet.2020.108200.

Kolby Smith W, Reed S C, Cleveland C C, et al. 2016. Large divergence of satellite and Earth system model estimates of global terrestrial CO_2 fertilization. Nature Climate Change, 6(3): 306–310.

Leng Y, Li W, Ciais P, et al. 2024. Forest aging limits future carbon sink in China. One Earth, 7(5): 822–834.

Li Y F, Zhang X, Wang B Y, et al. 2023. Revegetation promotes soil mineral-associated organic carbon sequestration and soil carbon stability in the Tengger Desert, northern China. Soil Biology and Biochemistry, 185: 109155, doi: 10.1016/j.soilbio.2023.109155.

Li Y P, Chen Y N, Sun F, et al. 2021. Recent vegetation browning and its drivers on Tianshan Mountain, Central Asia. Ecological Indicators, 129: 107912, doi: 10.1016/j.ecolind.2021.107912.

Liu J, Chen J M, Cihlar J, et al. 1997. A process-based boreal ecosystem productivity simulator using remote sensing inputs. Remote Sensing of Environment, 62(2): 158–175.

Mahecha M D, Reichstein M, Carvalhais N, et al. 2010. Global convergence in the temperature sensitivity of respiration at ecosystem level. Science, 329(5993): 838–840.

Min X Y, Zhang B Z, Wang Y S. 2025. Mining activities drive the temporal and spatial changes of ecosystem carbon storage in coal resource-based city with high groundwater table. Habitat International, 161: 103420, doi: 10.1016/j.habitatint.2025.103420.

Piao S L, Wang X H, Park T, et al. 2020. Characteristics, drivers and feedbacks of global greening. Nature Reviews Earth & Environment, 1(1): 14–27.

Raich J W, Potter C S, Bhagawati D. 2002. Interannual variability in global soil respiration, 1980–1994. Global Change Biology, 8(8): 800–812.

Ren Z G, Tian Z H, Wei H T, et al. 2022. Spatiotemporal evolution and driving mechanisms of vegetation in the Yellow River Basin, China during 2000–2020. Ecological Indicators, 138: 108832, doi: 10.1016/j.ecolind.2022.108832.

Reynolds J F, Smith D M S, Lambin E F, et al. 2007. Global desertification: Building a science for dryland development. Science, 316(5826): 847–851.

Ryu Y, Baldocchi D D, Kobayashi H, et al. 2011. Integration of MODIS land and atmosphere products with a coupled-process model to estimate gross primary productivity and evapotranspiration from 1 km to global scales. Global Biogeochemical Cycles, 25(4): GB4017, doi: 10.1029/2011GB004053.

Ryu Y, Berry J A, Baldocchi D D. 2019. What is global photosynthesis? History, uncertainties and opportunities. Remote Sensing of Environment, 223: 95–114.

Scurlock J M O, Hall D O. 1998. The global carbon sink: A grassland perspective. Global Change Biology, 4(2): 229–233.

Shi H, Li L H, Eamus D, et al. 2017. Assessing the ability of MODIS EVI to estimate terrestrial ecosystem gross primary production of multiple land cover types. Ecological Indicators, 72: 153–164.

Tu H Y, Jiapaer G, Yu T, et al. 2023. Effects of land cover change on vegetation carbon source/sink in arid terrestrial ecosystems of Northwest China, 2001–2018. Remote Sensing, 15(9): 2471, doi: 10.3390/rs15092471.

Wang Y G, Luo G P, Li C F, et al. 2025. Grazing weakens the carbon sequestration capacity of dry temperate grassland ecosystems in Central Asia. CATENA, 248: 108608, doi: 10.1016/j.catena.2024.108608.

Woodwell G M, Whittaker R H, Reiners W A, et al. 1978. The biota and the world carbon budget. Science, 199(4325): 141–146.

Wu G H, Guan K Y, Jiang C Y, et al. 2020. Radiance-based NIRv as a proxy for GPP of corn and soybean. Environmental Research Letters, 15(3): 034009, doi: 10.1088/1748-9326/ab65cc.

Xie W, Chen S T, Hu Z H. 2014. Factors influencing the variation of soil heterotrophic respiration in terrestrial ecosystems in China. Environmental Science, 35(1): 334–340. (in Chinese)

Xu L, Yu G R, He N P, et al. 2018. Carbon storage in China's terrestrial ecosystems: A synthesis. Scientific Reports, 8(1): 2806, doi: 10.1038/s41598-018-20764-9.

Yu G R, Chen Z, Piao S L, et al. 2014. High carbon dioxide uptake by subtropical forest ecosystems in the East Asian monsoon region. Proceedings of the National Academy of Sciences, 111(13): 4910–4915.

Yue X, Zhou H, Cao Y, et al. 2024. Large potential of strengthening the land carbon sink in China through anthropogenic interventions. Science Bulletin, 69(16): 2622–2631.

Zhang L F, Fang C L, Zhu C, et al. 2022. Ecosystem service trade-offs and identification of eco-optimal regions in urban agglomerations in arid regions of China. Journal of Cleaner Production, 373: 133823, doi: 10.1016/j.jclepro.2022.133823.

Zhang S R, Bai X Y, Zhao C W, et al. 2021. Global CO_2 consumption by silicate rock chemical weathering: Its past and future. Earth's Future, 9(5): e2020EF001938, doi: 10.1029/2020EF001938.

Zhang W Q, Luo G P, Yuan X L, et al. 2023. New data-driven method for estimation of net ecosystem carbon exchange at meteorological stations effectively increases the global carbon flux data. Methods in Ecology and Evolution, 14(9): 2449–2463.

Zhao M S, Running S W. 2010. Drought-induced reduction in global terrestrial net primary production from 2000 through 2009. Science, 329(5994): 940–943.